Available online at www.sciencedirect.com
SCIENCE DIRECT
C. R. Mecanique 333 (2005) 17–28
COMPTES RENDUS MECANIQUE
http://france.elsevier.com/direct/CRAS2B/

High-Order Methods for the Numerical Simulation of Vortical and Turbulent Flows

A fourth order accurate finite volume scheme for numerical simulations of turbulent Rayleigh–Bénard convection in cylindrical containers

Olga Shishkina *, Claus Wagner

DLR – Institute for Aerodynamics and Flow Technology, Bunsenstrasse 10, 37073 Göttingen, Germany

Available online 4 January 2005

Abstract

A finite volume scheme, which is based on fourth order accurate central differences in spatial directions and on a hybrid explicit/semi-implicit time stepping scheme, was developed to solve the incompressible Navier–Stokes and energy equations on cylindrical staggered grids. This includes a new fourth order accurate discretization of the velocity and temperature fields at the singularity of the cylindrical coordinate system and a new stability condition [J. Appl. Numer. Anal. Comput. Math. 1 (2004) 315–326]. The method was applied in direct numerical simulations of turbulent Rayleigh–Bénard convection for different Rayleigh numbers $Ra = 10^{\gamma}$, $\gamma = 5, \ldots, 8$, in wide cylinders with the aspect ratios $a \equiv H/R = 0.2$ and $a = 0.4$ (where R denotes the radius and H – the height of the cylinder). ***To cite this article: O. Shishkina, C. Wagner, C. R. Mecanique 333 (2005).***

Keywords: Computational fluid mechanics; Rayleigh–Bénard convection; Direct numerical simulation; High-order finite volume schemes

1. Introduction

Rayleigh–Bénard convection develops in fluid layers confined by two horizontal plates if the temperature difference between the lower heated and the upper cooled plate is high enough. The relevant dimensionless number $Ra = g\alpha H^3 \Delta T/\kappa\nu$, where g denotes the gravitational acceleration, α the thermal expansion coefficient, ΔT the temperature difference, κ the thermal diffusivity and ν the kinematic viscosity, is the Rayleigh number. Considering a specific fluid, the Rayleigh number can be increased if either the distance H between the two plates or their temperature difference ΔT is increased. Since Heslot [1], who performed an experiment in a cylindrical cell of the aspect ratio $a = H/R = 4$, it is known that Rayleigh–Bénard convection develops into a fully developed turbulent

* Corresponding author.
E-mail addresses: Olga.Chichkina@dlr.de (O. Shishkina), Claus.Wagner@dlr.de (C. Wagner).

1631-0721/$ – see front matter
doi:10.1016/j.crme.2004.09.020

state if Ra exceeds 10^7. In many experiments conducted to investigate turbulent Rayleigh–Bénard convection it was found that the heat transport expressed by the dimensionless Nusselt number Nu can be predicted in terms of the Rayleigh number by the scaling law $Nu = CRa^{\zeta}$ [2,3]. However, in a review article, Chavanne et al. [4] compared numerous experimental results and showed that the parameters C and ζ in the above scaling law depend on the aspect ratio a and the Prandtl number $Pr = \nu/\kappa$ of the fluid. Further, in [5], Grossmann and Lohse identified four different regions, where the Nusselt number Nu shows different scaling behavior with respect to Rayleigh and Prandtl numbers. Our objective is to investigate turbulent Rayleigh–Bénard convection in cylinders with the aspect ratio $a < 1$ by means of Direct Numerical Simulation (DNS).

While most experiments used a cylindrical confinement because of practical reasons, the majority of the conducted numerical simulations were done in planar configurations, as in Kimmel and Domaradzki [6], Grötzbach [7], Kerr [8]. Recently Verzicco and Camussi [9] presented results of marginally resolved DNS in a cylinder of the aspect ratio $a = 4$ for Rayleigh numbers up to 10^{11} using a second order accurate central difference code. Since Eggels et al. [10] and Unger [11], who investigated a turbulent pipe flow by means of DNS utilizing second order accurate central differences in space, it is known that second order differences provide reliable results (compared with experimental data) if statistical moments of order up to two are considered. Choi [12] confirmed that second order central schemes provide spectral-like accurate first and second order statistical moments, but for accurate predictions of higher order moments higher order spatial discretization schemes are needed. The order of discretization becomes more important if the Large Eddy Simulation (LES) technique is used. It was shown by Kravchenko and Moin [13] that subgrid scale models are effective only if central discretization of order higher than two is employed.

Having this in mind, we developed a finite volume method for solving the Navier–Stokes equations in cylindrical domains, which is based on fourth order accurate central differences in space. The method was applied in DNS of turbulent Rayleigh–Bénard convection in wide cylinders with aspect ratios of $a = 0.2$ and $a = 0.4$.

The structure of this article is the following. The governing differential equations and their discretized analogue are discussed in Section 2. We use the volume balance procedure of Schumann [14,15] to construct a finite volume form of the incompressible dimensionless Navier–Stokes equation in cylindrical coordinates (z, φ, r) on a staggered grid and consider different time discretization methods to solve the transport equations, namely, the explicit, semi-implicit and a hybrid explicit/semi-implicit time integration schemes. The last scheme is explicit in the bulk of the domain. Only in a thin subdomain around the cylinder axis those convection and viscous terms, which contain derivatives in circumferential φ-direction, are treated semi-implicitly. This approach provides stable calculations using time steps up to 5×10^2 times larger than with fully explicit schemes. In Section 3 we construct a fourth order accurate discretization scheme to compute the velocity and temperature fields and their partial derivatives on the surfaces of each finite volume. In Section 4 an algorithm developed to ensure fourth order accuracy at the singularity of a cylindrical coordinate system is presented. The algorithm provides smooth behaviour of all flow variables and their higher order statistical moments at the cylinder axis. Numerical experiments are discussed in Section 5. Based on results of a computation of laminar flow in a cylindrical annulus the order of the method is demonstrated. Further, presented DNS results of Rayleigh–Bénard convection include instantaneous flow characteristics, mean flow fields for different Rayleigh numbers and aspect ratios and the dependence of the Nusselt number on the Rayleigh number. Finally, a short analysis of the spatial and the temporal resolution requirements is given at the end of this section.

2. The governing equations and the numerical method

The governing equations for the Rayleigh–Bénard problem can be written as follows

$$\nabla \cdot \hat{\mathbf{u}} = 0, \quad \hat{\mathbf{u}}_t + \hat{\mathbf{u}} \cdot \nabla \hat{\mathbf{u}} + \rho^{-1} \nabla \hat{p} = \nu \nabla^2 \hat{\mathbf{u}} + \alpha g (\widehat{T} - \widehat{T}_0)\mathbf{z}, \quad \widehat{T}_0 = (\widehat{T}_1 + \widehat{T}_2)/2 \tag{1}$$
$$\widehat{T}_t + \hat{\mathbf{u}} \cdot \nabla \widehat{T} = \kappa \nabla^2 \widehat{T}$$

where $\hat{\mathbf{u}}$ is the velocity vector and $\hat{\mathbf{u}}_t$ is its time derivative, $\widehat{T}$ is the temperature field, $\widehat{T}_1$ and $\widehat{T}_2$ are the temperature values at the bottom and at the top of the cylinder and ρ is the density. In order to construct equations in dimensionless variables we introduce the reference values $x_b = R$, $t_b = x_b/u_b$, $u_b = \sqrt{\alpha g x_b \Delta T}$, $p_b = u_b^2\rho$, $T_b = \Delta T$ and represent each variable $\hat{\psi}$ as $\hat{\psi} = \psi_b\psi$, where ψ_b is the reference value and ψ is the dimensionless variable. Thus, from equations (1) the following system of dimensionless equations is obtained

$$\nabla\cdot\mathbf{u} = 0, \quad \mathbf{u}_t + \mathbf{u}\cdot\nabla\mathbf{u} + \nabla p = Gr^{-1/2}\nabla^2\mathbf{u} + T\mathbf{z} \tag{2}$$

$$T_t + \mathbf{u}\cdot\nabla T = Gr^{-1/2}Pr^{-1}\nabla^2 T \tag{3}$$

where $Pr = 0.7$ (for air) and $Gr = Ra/(a^3 Pr)$ is the Grashof number. On the cylinder walls the velocity field vanishes. The dimensionless temperature T varies from $+0.5$ at the bottom wall to -0.5 at the top wall of the cylinder. Further, an adiabatic vertical wall is prescribed by $\partial T/\partial r = 0$.

In order to generate a finite volume analogue of Eqs. (2) in cylindrical coordinates (z, φ, r) on a staggered grid we use Schumann's [14,15] volume balance procedure. The obtained finite volume equations are usually solved with algorithms based on Chorin's projection method (see [16] and [17]). This method includes three main steps. First, some auxiliary velocity field is calculated from equations obtained from the momentum equations (2) by neglecting the pressure term. Then, an elliptic Poisson equation is solved to satisfy the continuity equation. Finally, the velocity and pressure fields are updated using the auxiliary fields and the solution of the elliptic equation.

We consider a finite volume $V = V(z_i, \varphi_j, r_k)$ with the center (z_i, φ_j, r_k), which is bounded by the cell surfaces $A_z^{\pm} = A_z(z_i \pm \frac{\Delta z_i}{2}, \varphi_j, r_k)$, $A_\varphi^{\pm} = A_\varphi(z_i, \varphi_j \pm \frac{\Delta\varphi_j}{2}, r_k)$, $A_r^{\pm} = A_r(z_i, \varphi_j, r_k \pm \frac{\Delta r_k}{2})$, where Δz_i, $\Delta\varphi_j$, Δr_k are the sizes of the finite volume V in directions z, φ, r, respectively. Here we assume that each finite volume and its cell surfaces are associated with the coordinates of their own centers. The values ${}^{\beta^{\pm}}\overline{u_\alpha^n}$ and $\overline{u_\alpha^n}$ denote the velocity component u_α calculated for the time step number n and averaged over the $A_{\beta^{\pm}}$-surface and over the finite volume V, respectively. We use the notations $\Delta V = r_k\Delta r_k\Delta z_i\Delta\varphi_j$, $\Delta A_z = r_k\Delta r_k\Delta\varphi_j$, $\Delta A_\varphi = \Delta r_k\Delta z_i$, $\Delta A_r = r_k\Delta z_i\Delta\varphi_j$ and Δt for the time step.

2.1. Explicit scheme

Integrating Eq. (2) over the finite volume V and using the explicit Leapfrog time integration scheme, we obtain the following equations:

$$\frac{\overline{u_\alpha^{n+1}} - \overline{u_\alpha^{n-1}}}{2\Delta t} + \sum_{\beta=z,\varphi,r}\left(K_{\alpha\beta}^{n,n} - D_{\alpha\beta}^{n-1,n-1}\right) + P_\alpha^n - C_\alpha^n = 0, \quad \alpha = z,\varphi,r \tag{4}$$

where
$K_{\alpha\beta}^{n,m} = \frac{1}{\Delta V}(\Delta A_\beta^{+}\,{}^{\beta^+}\overline{u_\alpha^n}\,{}^{\beta^+}\overline{u_\beta^m} - \Delta A_\beta^{-}\,{}^{\beta^-}\overline{u_\alpha^n}\,{}^{\beta^-}\overline{u_\beta^m})$ denotes the convective term,
$D_{\alpha\beta}^{n,m} = \frac{1}{\sqrt{Gr}\Delta V}(\Delta A_\beta^{+}\,{}^{\beta^+}\overline{s_{\alpha\beta}^{n,m}} - \Delta A_\beta^{-}\,{}^{\beta^-}\overline{s_{\alpha\beta}^{n,m}})$ the diffusive term,
$P_\alpha^n = \frac{1}{\Delta V}(\Delta A_\alpha^{+}\,{}^{\alpha^+}\overline{p^n} - \Delta A_\alpha^{-}\,{}^{\alpha^-}\overline{p^n})$ the pressure term,
$C_z^n = 0$, $C_\varphi^n = \frac{\Delta\varphi_j\Delta A_\varphi}{\Delta V}(-{}^{\varphi}\overline{u_\varphi^n}\,{}^{\varphi}\overline{u_r^n} + \nu^{\varphi}\overline{s_{\varphi r}^n})$, $C_r^n = \frac{\Delta\varphi_j\Delta A_\varphi}{\Delta V}(({}^{\varphi}\overline{u_\varphi^n})^2 + {}^{\varphi}\overline{p^n} - \nu\,{}^{\varphi}\overline{s_{\varphi\varphi}^n})$ the curvature terms and

$${}^{\beta}\overline{s_{\alpha\beta}^{n,m}} = \begin{bmatrix} 2\dfrac{\partial}{\partial z}{}^{z}\overline{u_z^n} & \dfrac{1}{r}\dfrac{\partial}{\partial\varphi}{}^{\varphi}\overline{u_z^m} + \dfrac{\partial}{\partial z}{}^{\varphi}\overline{u_\varphi^n} & \dfrac{\partial}{\partial r}{}^{r}\overline{u_z^n} + \dfrac{\partial}{\partial z}{}^{r}\overline{u_r^n} \\ \dfrac{1}{r}\dfrac{\partial}{\partial\varphi}{}^{\varphi}\overline{u_z^m} + \dfrac{\partial}{\partial z}{}^{\varphi}\overline{u_\varphi^n} & \dfrac{1}{r}\left(\dfrac{\partial}{\partial\varphi}{}^{\varphi}\overline{u_\varphi^n} + {}^{\varphi}\overline{u_\varphi^m}\right) + \dfrac{2}{r}{}^{\varphi}\overline{u_r^n} & r\dfrac{\partial}{\partial r}\left({}^{r}\overline{u_\varphi^n}/r\right) + \dfrac{1}{r}\dfrac{\partial}{\partial\varphi}{}^{r}\overline{u_r^m} \\ \dfrac{\partial}{\partial r}{}^{r}\overline{u_z^n} + \dfrac{\partial}{\partial z}{}^{r}\overline{u_r^n} & r\dfrac{\partial}{\partial r}\left({}^{r}\overline{u_\varphi^n}/r\right) + \dfrac{1}{r}\dfrac{\partial}{\partial\varphi}{}^{r}\overline{u_r^m} & 2\dfrac{\partial}{\partial r}{}^{r}\overline{u_r^n} \end{bmatrix}$$

the deformation tensor.

The solution of Eq. (4) is obtained in three steps. First, an approximate velocity field $\mathbf{u}^* = (u_z^*, u_\varphi^*, u_r^*)$ is computed from equations similar to and obtained from Eq. (4) by neglecting the pressure term

$$\frac{\overline{u_\alpha^*} - \overline{u_\alpha^{n-1}}}{2\Delta t} + \sum_{\beta=z,\varphi,r} \left(K_{\alpha\beta}^{n,n} - D_{\alpha\beta}^{n-1,n-1}\right) - C_\alpha^n = 0, \quad \alpha = z, \varphi, r \tag{5}$$

On solid walls the approximate velocity field is set to zero, $\overline{u_\alpha^*} = 0$, $\alpha = z, \varphi, r$, according to the no-slip and impermeability boundary conditions. Then the Poisson equation

$$\nabla^2 \overline{\phi^n} = \frac{1}{\Delta V} \sum_{\beta=z,\varphi,r} \left(\Delta A_\beta^{+\,\beta^+} \overline{u_{\beta^+}^*} - \Delta A_\beta^{-\,\beta^-} \overline{u_{\beta^-}^*}\right) \tag{6}$$

is solved to calculate an auxiliary function $\overline{\phi^n}$, which satisfies the equality $\mathbf{n} \cdot \nabla \overline{\phi^n} = 0$ on solid walls ($\mathbf{n}$ is the normal vector). Finally, the velocity field and the pressure are updated as follows:

$$\overline{\mathbf{u}^{n+1}} = \overline{\mathbf{u}^*} - \nabla \overline{\phi^n}, \qquad \overline{p^n} = \frac{\overline{\phi^n}}{2\Delta t} \tag{7}$$

The finite volume equation for the temperature (3) is derived analogously.

2.2. Semi-implicit scheme

In cylindrical coordinates explicit treatment of the viscous term $D_{\alpha\varphi}^{n-1,n-1}$ and the convective term $K_{\alpha\varphi}^{n,n}$ leads to an extremely small time step in a thin subdomain around the cylinder axis. Therefore, in this subdomain we apply implicit time stepping in φ-direction,

$$\frac{\overline{u_\alpha^{n+1}} - \overline{u_\alpha^{n-1}}}{2\Delta t} + \sum_{\beta=z,r} \left(K_{\alpha\beta}^{n,n} - D_{\alpha\beta}^{n-1,n-1}\right) + K_{\alpha\varphi}^{n+1,n} - D_{\alpha\varphi}^{n-1,n+1} + P_\alpha^n - C_\alpha^n = 0, \quad \alpha = z, \varphi, r \tag{8}$$

The solution process for (8) is the same as for (4). First, an approximate velocity field $\mathbf{u}^* = (u_z^*, u_\varphi^*, u_r^*)$ is calculated solving

$$\frac{\overline{u_\alpha^*} - \overline{u_\alpha^{n-1}}}{2\Delta t} + \sum_{\beta=z,r} \left(K_{\alpha\beta}^{n,n} - D_{\alpha\beta}^{n-1,n-1}\right) + K_{\alpha\varphi}^{*,n} - D_{\alpha\varphi}^{n-1,*} - C_\alpha^n = 0, \quad \alpha = z, \varphi, r$$

with any fast band matrices solver. Then, the Poisson Eq. (6) is solved and the velocity field (7) is updated, but now the pressure $\overline{p^n} = (\frac{1}{2\Delta t} + \overline{u_\varphi^n}\frac{\partial}{\partial\varphi} + \frac{\partial \overline{u_\varphi^n}}{\partial\varphi} - \nu\frac{\partial^2}{\partial\varphi^2})\overline{\phi^n}$, as discussed in [18].

2.3. Hybrid explicit/semi-implicit time stepping

For stable calculations the time step Δt must be smaller than the critical time step. The latter can be derived by means of the von Neumann stability analysis. In [19] the critical time step valid for the Leapfrog–Euler scheme (5) together with spatial central differences of any even order was derived. In particular, for the case $Pr < 1$, an equidistant mesh and fourth order accurate central differences (10), (11) the sufficient condition for the stability can be written as follows (see also [20]):

$$\Delta t < \Delta t_{\text{exp}}^{\text{crit}} = \left(\frac{3}{2}\sum_{\beta=1}^{3}\frac{U_\beta}{\Delta x_\beta} + \frac{16}{3\sqrt{Gr}\,Pr}\sum_{\beta=1}^{3}\frac{1}{\Delta x_\beta^2}\right)^{-1}$$

where $\Delta x_\beta = \Delta\beta$ for $\beta = r, z$ and $\Delta x_\varphi = r\Delta\varphi$. The component of the velocity field U_β in the von Neumann stability analysis is supposed to be constant. Since the von Neumann analysis is applicable only for linear problems, we multiply the value $\Delta t_{\rm exp}^{\rm crit}$ by the safety factor 0.5 to avoid nonlinear instabilities. Thus, for stable solutions of (5) with fourth order accurate central differences in space the critical time step equals

$$\begin{aligned}
&\Delta t_{\rm exp}^{\rm crit} = 0.5/\widehat{\Sigma}_{\rm exp}\\
&\widehat{\Sigma}_{\rm exp} = \max_{z_i,\varphi_j,r_k}\left\{\frac{3}{2}\left(\frac{\overline{u_z}(z_i+0.5\Delta z_i,\varphi_j,r_k)}{\Delta z_i}+\frac{\overline{u_\varphi}(z_i,\varphi_j+0.5\Delta\varphi_j,r_k)}{r_k\Delta\varphi_j}+\frac{\overline{u_r}(z_i,\varphi_j,r_k+0.5\Delta r_k)}{\Delta r_k}\right)\right.\\
&\qquad\left.+\frac{16}{3\sqrt{Gr}Pr}\left(\frac{1}{\Delta z_i^2}+\frac{1}{(r_k\Delta\varphi_j)^2}+\frac{1}{\Delta r_k^2}\right)\right\}
\end{aligned}\tag{9}$$

The sum $\widehat{\Sigma}_{\rm exp}$ can be estimated as $\widehat{\Sigma}_{\rm exp} \leqslant \Sigma_{\rm exp} = \max_{r_k}\sum_{\beta=z,\varphi,r}\{S_\beta^d + S_\beta^c\}$, where

$$\begin{aligned}
S_z^d &= \frac{16}{3\sqrt{Gr}Pr}\max_{z_i}\frac{1}{(\Delta z_i)^2}\\
S_\varphi^d &= \frac{16}{3\sqrt{Gr}Pr}\max_{\varphi_j}\frac{1}{(r_k\Delta\varphi_j)^2}\\
S_r^d &= \frac{16}{3\sqrt{Gr}Pr}\frac{1}{(\Delta r_k)^2}\\
S_z^c &= \frac{3}{2}\max_{z_i,\varphi_j}\frac{|\overline{u_z}(z_i+0.5\Delta z_i,\varphi_j,r_k)|}{\Delta z_i}\\
S_\varphi^c &= \frac{3}{2}\max_{z_i,\varphi_j}\frac{|\overline{u_\varphi}(z_i,\varphi_j+0.5\Delta\varphi_j,r_k)|}{r_k\Delta\varphi_j}\\
S_r^c &= \frac{3}{2}\max_{z_i,\varphi_j}\frac{|\overline{u_r}(z_i,\varphi_j,r_k+0.5\Delta r_k)|}{\Delta r_k}
\end{aligned}$$

The critical time step, which guarantees the stability of the semi-implicit scheme in φ-direction (8), can be calculated from $\Delta t_{\rm imp}^{\rm crit} = 0.5/\widehat{\Sigma}_{\rm imp}$, $\widehat{\Sigma}_{\rm imp} \leqslant \Sigma_{\rm imp} = \max_{r_k}\sum_{\beta=z,r}\{S_\beta^d + S_\beta^c\}$.

In Fig. 1 S_β^d and S_β^c ($\beta = z, \varphi, r$) are depicted as they were determined from an instantaneous velocity field $(\overline{u_z}, \overline{u_\varphi}, \overline{u_r})$ obtained for a certain time step in the DNS of Rayleigh–Bénard convection for $Ra = 10^5$ and $a = 0.2$.

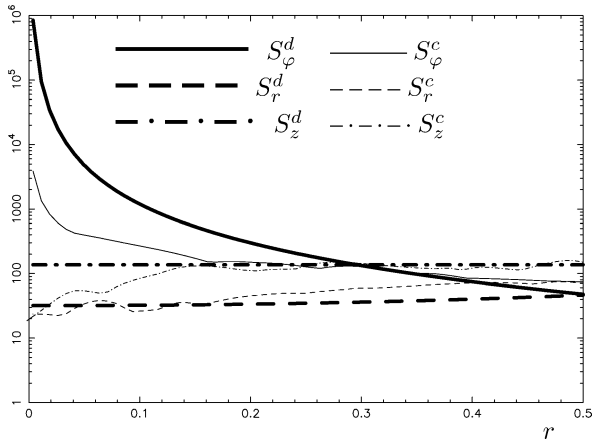

Fig. 1. Different items contributing to $\Sigma_{\rm exp}$.

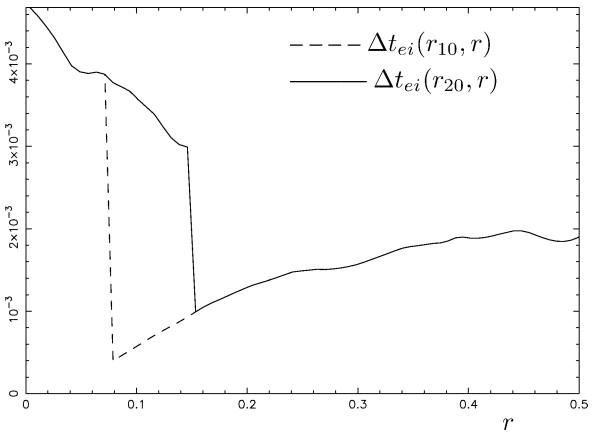

Fig. 2. Functions $\Delta t_{ei}(r_{10}, r)$ and $\Delta t_{ei}(r_{20}, r)$.

It can be observed that in the vicinity of the cylinder axis S_φ^d and S_φ^c are the leading terms in the sum $\Sigma_{\exp}$. The large values of S_φ^d and S_φ^c near $r=0$ force the critical time step in the explicit scheme to be very small. To overcome this, we propose to use the explicit scheme (4) in the bulk of the cylindrical domain and the semi-implicit scheme (8) close to the cylinder axis, i.e. in those finite volumes, for which $r_k \leqslant r_\gamma$, $1 < \gamma < N_r$, where N_r denotes the number of grid points in r-direction. Then, the critical time step can be computed as follows:

$$\Delta t_{ei}^{\text{crit}}(r_\gamma) = \min_{r_k} \Delta t_{ei}(r_\gamma, r_k), \quad \Delta t_{ei}(r_\gamma, r_k) = 0.5\big(S_z^d + S_z^c + S_r^d + S_r^c + (S_\varphi^d + S_\varphi^c)\xi(\gamma, k)\big)^{-1}$$

where $\xi(\gamma, k) = 0$, if $r_k \leqslant r_\gamma$; $\xi(\gamma, k) = 1$, if $r_k > r_\gamma$.

In Fig. 2 the function $\Delta t_{ei}(r_\gamma, r_k)$ is depicted for $\gamma = 10$ and $\gamma = 20$. For the DNS of Rayleigh–Bénard convection ($Ra = 10^5$, $a = 0.2$) we used $\gamma = 20$ and obtained $\Delta t_{ei}^{\text{crit}} \approx 5 \times 10^{-4}$. Note, that on the same grid the fully explicit scheme (4) leads to $\Delta t_{\exp}^{\text{crit}} < 10^{-6}$.

3. Fourth order central discretization

In this section we construct a fourth order accurate approximation scheme to compute the value ${}^\beta\overline{u_\alpha}$ and its partial derivatives $\frac{\partial}{\partial\beta}\,{}^\beta\overline{u_\alpha}$, $\alpha = z, \varphi, r$; $\beta = z, \varphi, r$. These averaged values have to be determined in order to close the system of equations. The accuracy of the here chosen approximation determines the spatial accuracy of the solution and influences significantly the precision of high order statistical moments.

Let β be one of the coordinates (z, φ or r). For simplicity variation in β-direction only is considered in this section, while the other two coordinates are assumed to be constant. Therefore, we omit everywhere the other two coordinates and consider a certain number of finite volumes $V(\beta_i)$, $i \in N$, bounded by the surfaces $A_\beta(\beta_i - \frac{\Delta\beta_i}{2})$ and $A_\beta(\beta_i + \frac{\Delta\beta_i}{2})$, where $\Delta\beta_i$ is the size of the finite volume $V(\beta_i)$ in the direction β. The values $\overline{u_\alpha}(\beta_i)$ and ${}^\beta\overline{u_\alpha}(\beta_i + \frac{\Delta\beta_i}{2})$ denote the u_α-component averaged over $V(\beta_i)$ and $A_\beta(\beta_i + \frac{\Delta\beta_i}{2})$, respectively.

An approximation scheme for ${}^\beta\overline{u_\alpha}(\beta_i + \frac{\Delta\beta_i}{2})$ and $\frac{\partial}{\partial\beta}\,{}^\beta\overline{u_\alpha}(\beta_i + \frac{\Delta\beta_i}{2})$ involves a certain number of values $\overline{u_\alpha}(\beta_{i\pm k})$, $k \in N$. In order to avoid an unpleasant property of non-central schemes, i.e. the dissipativity, we use central differences everywhere except in the near wall region. Further, we assume that the component u_α averaged over $A_\beta(\beta)$ equals some polynomial of the coordinate β, i.e. ${}^\beta\overline{u_\alpha}(\beta) = \sum_{k=1}^4 \zeta_k \beta^{k-1}$, where ζ_k, $k = 1, 2, 3, 4$, are some coefficients. From this one can compute the volume-averaged value of u_α as follows

$$\overline{u_\alpha}(\beta_j) = \frac{1}{\Delta\beta_j} \int_{\beta_j - \Delta\beta_j/2}^{\beta_j + \Delta\beta_j/2} {}^\beta\overline{u_\alpha}(\beta)\,\mathrm{d}\beta, \quad \beta = z, \varphi, \quad \overline{u_\alpha}(r_j) = \frac{1}{r_j\,\Delta r_j} \int_{r_j - \Delta r_j/2}^{r_j + \Delta r_j/2} r \cdot {}^r\overline{u_\alpha}(r)\,\mathrm{d}r, \quad \beta = r,\ \alpha = z, \varphi, r$$

Calculation of the values $\overline{u_\alpha}(\beta_j)$ for $j = i-1, i, i+1, i+2$ leads to a system of linear equations for the coefficients ζ_k, $k = 1, 2, 3, 4$. Solving this system one can approximate the values of ${}^\beta\overline{u_\alpha}(\beta)$ and $\frac{\partial}{\partial\beta}\,{}^\beta\overline{u_\alpha}(\beta)$ for any $\beta \in [\beta_{i-1}, \beta_{i+2}]$, in particular, near solid walls. For example, for equidistant meshes with $\Delta\beta_i = \Delta$ in directions $\beta = z, \varphi$ the approximation scheme can be written:

$${}^\beta\overline{u_\alpha}\left(\beta_i + \frac{\Delta}{2}\right) = \big[-\overline{u_\alpha}(\beta_{i-1}) + 7\overline{u_\alpha}(\beta_i) + 7\overline{u_\alpha}(\beta_{i+1}) - \overline{u_\alpha}(\beta_{i+2})\big]/12 \tag{10}$$

$$\frac{\partial}{\partial\beta}\,{}^\beta\overline{u_\alpha}\left(\beta_i + \frac{\Delta}{2}\right) = \big[\overline{u_\alpha}(\beta_{i-1}) - 15\overline{u_\alpha}(\beta_i) + 15\overline{u_\alpha}(\beta_{i+1}) - \overline{u_\alpha}(\beta_{i+2})\big]/12\Delta \tag{11}$$

4. Calculation of the velocity field at the cylinder axis

Determining the velocity field at the singularity of the cylindrical coordinate system is one of the cornerstones of numerical simulations (see, for example, Mitchell et al. [21] and Mohseni, Colonius [22]). In this section we derive an algorithm to compute the values ${}^r\overline{u_z}(z_i,\varphi_j,0)$ and ${}^r\overline{u_\alpha}(z_i,\varphi_j,r_0)$, $\alpha=\varphi,r$, for $r_0\to 0$. As previously, an equidistant mesh is considered in order to simplify the description. For non-equidistant grids the calculations can be done analogously. Let $z_i=(i-0.5)\Delta z$ for $i=1,\dots,N_z$ and $N_z\Delta z=H/x_b=a$; $\varphi_j=(j-0.5)\Delta\varphi$ for $j=1,\dots,N_\varphi$ and $N_\varphi\Delta\varphi=2\pi$; $r_k=(k-0.5)\Delta r$ for $k=1,\dots,N_r$ and $N_r\Delta r=R/x_b=1$.

4.1. Calculation of the axial velocity component

From Eq. (10) we obtain

$$
\begin{aligned}
{}^r\overline{u_z^*}(z_i+0.5\Delta z,\varphi_j,0)=\big[&-\overline{u_z}(z_i+0.5\Delta z,\varphi_j+\pi,r_2)+7\overline{u_z}(z_i+0.5\Delta z,\varphi_j+\pi,r_1)\\
&+7\overline{u_z}(z_i+0.5\Delta z,\varphi_j,r_1)-\overline{u_z}(z_i+0.5\Delta z,\varphi_j,r_2)\big]/12,\quad j=1,\dots,N_\varphi/2
\end{aligned}
$$

which represents the interpolation across the cylinder axis. In order to obtain the unique value ${}^r\overline{u_z}$ at the singularity $r=0$ we apply averaging in φ-direction.

$$
\textit{Step 1}:\quad {}^r\overline{u_z}(z_i+0.5\Delta z,\varphi_j,0)=\frac{1}{3N_\varphi}\sum_{l=1}^{N_\varphi/2}\big[7\overline{u_z}(z_i+0.5\Delta z,\varphi_l,r_1)-\overline{u_z}(z_i+0.5\Delta z,\varphi_l,r_2)\big],\quad j=1,\dots,N_\varphi
$$

4.2. Calculation of the azimuthal velocity component

Since $u_\varphi(z_i,\varphi_j+0.5\Delta\varphi,r_0)=-u_\varphi(z_i,\varphi_j+0.5\Delta\varphi+\pi,r_0)$ for $r_0\to 0$, $j=1,\dots,N_\varphi/2$, interpolation according to Eq. (10) leads to

$$
\begin{aligned}
\textit{Step 2}:\quad {}^r\overline{u_\varphi^*}(z_i,\varphi_j+0.5\Delta\varphi,r_0)=\big[&\overline{u_\varphi}(z_i,\varphi_j+0.5\Delta\varphi+\pi,r_2)-7\overline{u_\varphi}(z_i,\varphi_j+0.5\Delta\varphi+\pi,r_1)\\
&+7\overline{u_\varphi}(z_i,\varphi_j+0.5\Delta\varphi,r_1)-\overline{u_\varphi}(z_i,\varphi_j+0.5\Delta\varphi,r_2)\big]/12,\quad j=1,\dots,N_\varphi/2
\end{aligned}
$$

4.3. Calculation of the radial velocity component

The continuity equation in cylindrical coordinates can be written as $r(\frac{\partial u_z}{\partial z}+\frac{\partial u_r}{\partial r})+\frac{\partial u_\varphi}{\partial\varphi}+u_r=0$. The functions $\frac{\partial u_z}{\partial z}$, $\frac{\partial u_r}{\partial r}$ are bounded while $r\to 0$, hence, one can calculate an approximation to ${}^r\overline{u_r}(z_i,\varphi_j,r_0)$ with

$$
\textit{Step 3}:\quad {}^r\overline{u_r^*}(z_i,\varphi_j,r_0)=-\big({}^r\overline{u_\varphi^*}(z_i,\varphi_j+0.5\Delta\varphi,r_0)-{}^r\overline{u_\varphi^*}(z_i,\varphi_j-0.5\Delta\varphi,r_0)\big)/\Delta\varphi,\quad j=1,\dots,N_\varphi
$$

4.4. Calculation of the velocity components in Cartesian coordinates

Since the pairs $\{{}^r\overline{u_\varphi}(z_i,\varphi_j+0.5\Delta\varphi,r_0),\ {}^r\overline{u_r}(z_i,\varphi_j,r_0)\}$ for any j must describe the same Cartesian vector $\{U(z_i),V(z_i)\}$, we apply averaging in Cartesian coordinates in order to obtain the unique solution

$$
\textit{Step 4}:\quad U(z_i)=\frac{1}{N_\varphi}\sum_{j}^{N_\varphi}\big\{{}^r\overline{u_r^*}(z_i,\varphi_j,r_0)\cos\varphi_j-{}^r\overline{u_\varphi^*}(z_i,\varphi_j+0.5\Delta\varphi,r_0)\sin(\varphi_j+0.5\Delta\varphi)\big\}
$$

$$
V(z_i)=\frac{1}{N_\varphi}\sum_{j}^{N_\varphi}\big\{{}^r\overline{u_r^*}(z_i,\varphi_j,r_0)\sin\varphi_j+{}^r\overline{u_\varphi^*}(z_i,\varphi_j+0.5\Delta\varphi,r_0)\cos(\varphi_j+0.5\Delta\varphi)\big\}
$$

4.5. Update of the azimuthal and the radial velocity components

From the Cartesian vector $\{U(z_i), V(z_i)\}$ we finally calculate the vectors in cylindrical coordinates for $r_0 \to 0$.

$$\textit{Step 5:}\quad {}^{r}\overline{u_r}(z_i, \varphi_j, r_0) = \big\{U(z_i)\cos(\varphi_j + 0.5\Delta\varphi) + V(z_i)\sin(\varphi_j + 0.5\Delta\varphi)\big\}/\cos\varphi_1$$
$${}^{r}\overline{u_\varphi}(z_i, \varphi_j + 0.5\Delta\varphi, r_0) = \big\{-U(z_i)\sin\varphi_j + V(z_i)\cos\varphi_j\big\}/\cos\varphi_1, \quad j = 1, \ldots, N_\varphi$$

With this algorithm the velocity field at the cylinder axis and in the bulk of cylinder can be computed with the same order of accuracy.

5. Numerical experiments

5.1. Laminar flow in a cylindrical annulus

Numerical simulations of some simple test cases were carried out to validate the method. One of them, the laminar flow in a cylindrical annulus of radiuses $R = 1$ and $R = 0.5$, is governed by the equation $\frac{1}{r}\frac{\mathrm{d}}{\mathrm{d}r}(r\frac{\mathrm{d}u_z}{\mathrm{d}r}) = -8$ with the general solution $u_z = -2r^2 + C_1 \ln r + C_2$. The constants C_1 and C_2 can be derived using the conditions $u_z|_{r=1} = 0$ ($C_2 = 2$) and $u_z|_{r=0.5} = 0$ ($C_1 = \frac{3}{2\ln 2}$). The resulting solution can be expressed: $u_z = 2(1 - r^2) + \frac{3\ln r}{2\ln 2}$.

Considering rings bounded by circles of radius $(r_i - \frac{\Delta r}{2})$ and $(r_i + \frac{\Delta r}{2})$, the ring averaged value of u_z is given by:

$$\overline{u_z}(r_i) = \frac{1}{r_i\,\Delta r}\int_{r_i-\Delta r/2}^{r_i+\Delta r/2} u_z r\,\mathrm{d}r = \frac{1}{2r_i\,\Delta r}\left(2r^2 - r^4 + \frac{3}{\ln 2}\left(\frac{r^2}{2}\ln r - \frac{r^2}{4}\right)\right)\Bigg|_{r_i-\Delta r/2}^{r_i+\Delta r/2}. \tag{12}$$

The corresponding simulations were performed on meshes with $N_z = 4$ and $N_\varphi = 4$ grid points in z- and φ-directions, respectively, and $N_r = 8, 16, 24, 32$ grid points in r-direction. The initial velocity field was put to zero. 16 400 time steps (for $N_r = 32$) were computed with a time step $\Delta t = 3.05 \times 10^{-3}$ until the convergence criterion

$$\big|\overline{u_z}(t + \Delta t) - \overline{u_z}(t)\big|\big|\overline{u_z}(t)\big|^{-1} < 4 \times 10^{-12}$$

was reached. The resulting mean error $\epsilon = \sum_{r_i} |\overline{u_{z,\mathrm{sim}}} - \overline{u_{z,\mathrm{anal}}}| r_i\,\Delta r$, where $\overline{u_{z,\mathrm{sim}}}$ is the value obtained in the simulations and $\overline{u_{z,\mathrm{anal}}}$ is the analytical solution (12), is presented in Fig. 3. For this test case second order accurate discretization provides ϵ no better than $\mathrm{O}((\Delta r)^{1.527})$, while fourth order discritization leads to $\epsilon \sim (\Delta r)^{3.866}$. Some details of the fourth order simulation, ($N_r = 32$, $\epsilon = 3.79 \times 10^{-8}$) are given in Table 1, where $\Delta = |\overline{u_{z,\mathrm{sim}}} - \overline{u_{z,\mathrm{anal}}}|$ and δ denotes the relative error $\delta = \Delta|\overline{u_{z,\mathrm{anal}}}|^{-1} \cdot 100\%$.

More results obtained in other test cases with the presented fourth order method can be found in [18].

5.2. Rayleigh–Bénard convection

DNS of turbulent Rayleigh–Bénard convection based on the proposed fourth order central differences (10), (11) in combination with the time stepping (9), were conducted as well. A cylindrical mesh, consisting of 110 and 512 equidistantly distributed points in the streamwise z- and azimuthal φ-directions, respectively, and 96 points in wall-normal r-direction, which were clustered in the vicinity of the wall, were used. The simulations were started in the quiescent state with a randomly disturbed linearly distributed mean temperature field $T(z, \varphi, r) = 0.5 - z/a$.

Table 1
Comparison of analytical and numerical solutions (obtained with the fourth order code for $N_r = 32$)

r_i	$\overline{u_{z,\mathrm{sim}}}$	$\overline{u_{z,\mathrm{anal}}}$	Δ	δ (%)
0.508	0.178E−01	0.178E−01	2.777E−07	1.563E−03
0.523	0.511E−01	0.511E−01	2.014E−07	3.940E−04
0.539	0.816E−01	0.816E−01	1.919E−07	2.353E−04
0.555	0.109E+00	0.109E+00	1.867E−07	1.709E−04
0.570	0.134E+00	0.134E+00	1.813E−07	1.351E−04
0.586	0.157E+00	0.157E+00	1.756E−07	1.122E−04
0.602	0.176E+00	0.176E+00	1.697E−07	9.623E−05
0.617	0.194E+00	0.194E+00	1.636E−07	8.443E−05
0.633	0.209E+00	0.209E+00	1.573E−07	7.535E−05
0.648	0.222E+00	0.222E+00	1.510E−07	6.815E−05
0.664	0.232E+00	0.232E+00	1.446E−07	6.230E−05
0.680	0.240E+00	0.240E+00	1.381E−07	5.745E−05
0.695	0.247E+00	0.247E+00	1.316E−07	5.337E−05
0.711	0.251E+00	0.251E+00	1.251E−07	4.991E−05
0.727	0.253E+00	0.253E+00	1.187E−07	4.694E−05
0.742	0.253E+00	0.253E+00	1.123E−07	4.437E−05
0.758	0.251E+00	0.251E+00	1.059E−07	4.215E−05
0.773	0.247E+00	0.247E+00	9.956E−08	4.022E−05
0.789	0.242E+00	0.242E+00	9.328E−08	3.855E−05
0.805	0.235E+00	0.235E+00	8.707E−08	3.711E−05
0.820	0.225E+00	0.225E+00	8.092E−08	3.589E−05
0.836	0.215E+00	0.215E+00	7.484E−08	3.489E−05
0.852	0.202E+00	0.202E+00	6.883E−08	3.410E−05
0.867	0.188E+00	0.188E+00	6.289E−08	3.354E−05
0.883	0.171E+00	0.171E+00	5.702E−08	3.326E−05
0.898	0.154E+00	0.154E+00	5.123E−08	3.332E−05
0.914	0.134E+00	0.134E+00	4.550E−08	3.385E−05
0.930	0.113E+00	0.113E+00	3.985E−08	3.512E−05
0.945	0.910E−01	0.910E−01	3.428E−08	3.768E−05
0.961	0.669E−01	0.669E−01	2.880E−08	4.306E−05
0.977	0.412E−01	0.412E−01	2.374E−08	5.757E−05
0.992	0.141E−01	0.141E−01	2.361E−08	1.680E−04

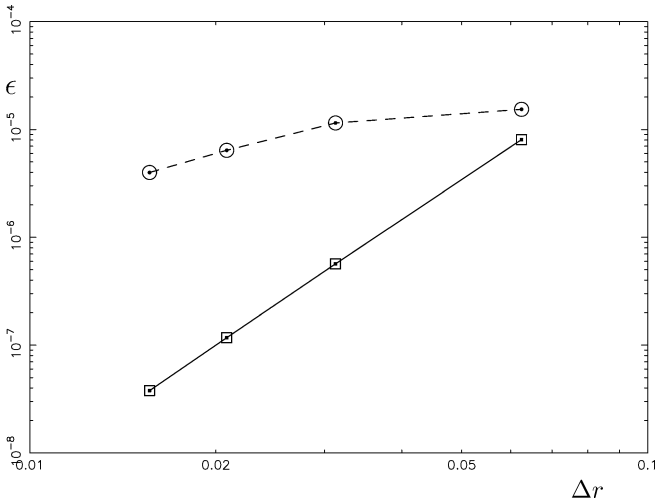

Fig. 3. Error ϵ versus the mesh size of 2nd order and 4th order code. ○ 2th order, $N_z = 4$, $N_\varphi = 4$; □ 4th order, $N_z = 4$, $N_\varphi = 4$.

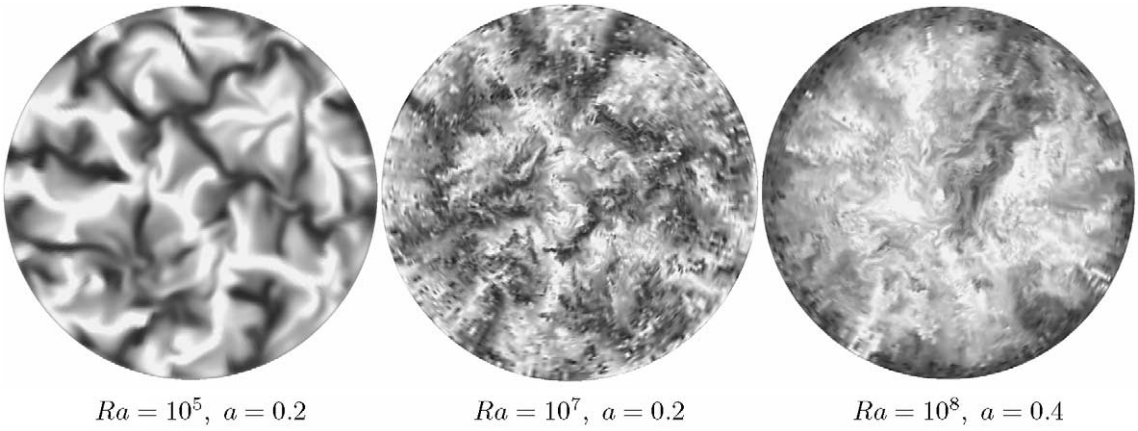

Fig. 4. Snapshots of the axial velocity field u_z in the cross-section $z = a/2$. Dark: $u_z < 0$, light: $u_z > 0$.

5.2.1. Instantaneous flow fields

In Fig. 4 snapshots of the axial velocity component in the central cross-section of the cylinder are depicted for different Rayleigh numbers and aspect ratios. Light tones correspond to positive values of the axial velocity component (the flow goes up) and dark tones to negative values. For the case $Ra = 10^5,\ a = 0.2$, elongated structures can be observed. If the Rayleigh number is increased to $Ra = 10^7$ fine flow structures evolve on top of these large structures leading to a more corrugated large scale flow. Further increasing the Rayleigh number to $Ra = 10^8$ in a cylinder with the higher aspect ratio $a = 0.4$, leads to a single large flow structure, in which warm fluid rises in the bulk and cold fluid descends close to the cylinder sidewall.

In Fig. 5 side views of isothermal surfaces for $T = 0.2$ and $T = 0.3$ are presented as they were obtained for $Ra = 10^5$ and $a = 0.2$. The isosurfaces are predominantly smooth, except in some narrow cracks. These regions

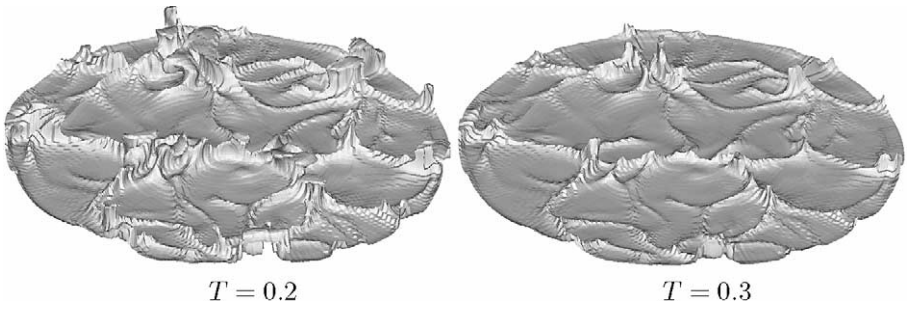

Fig. 5. Instantaneous isosurfaces of the temperature obtained for $Ra = 10^5$ and $a = 0.2$.

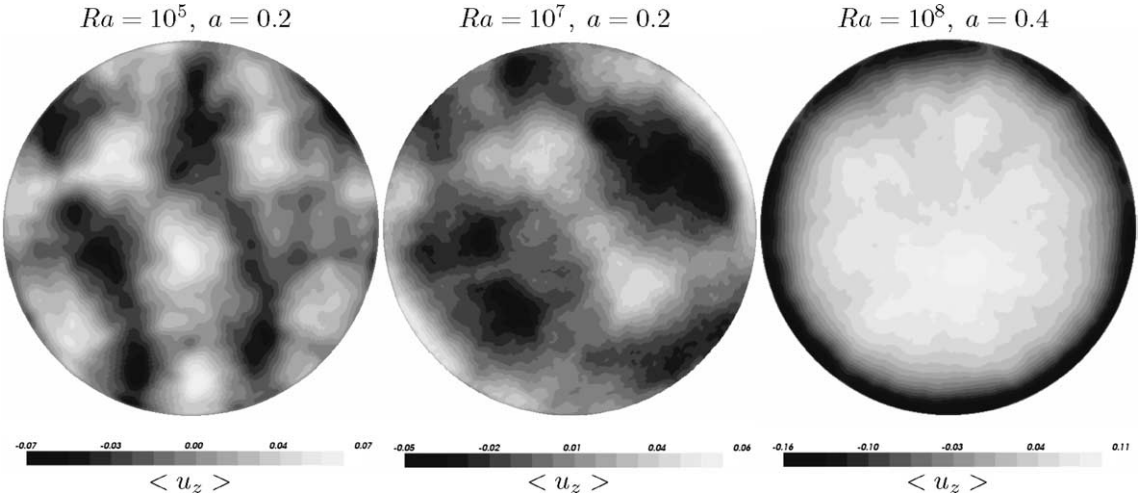

Fig. 6. Contours of the time averaged mean axial velocity components $\langle u_z \rangle$ in the cross-section $z = a/2$.

of comparably warm fluid can reach the top of the cylinder. The isotherms of the negative temperature values are similar in shape, i.e. they are almost flat, except in some cracks of cold flow ($T < 0$) that can reach the vicinity of the cylinder bottom.

5.2.2. Mean flow characteristics

In order to check, whether the observed instantaneous flow structures are statistically relevant, we conducted time averaging of the fully three-dimensional flow fields. In Fig. 6 the contours of the mean axial velocity component in the central horizontal cross-section of the cylinder are presented for three different Rayleigh numbers and two aspect ratios. The time averaging was performed over approximately 500 dimensionless time units until no significant change of the mean velocity maximum was observed. From the comparison of mean flow structures obtained for different *Ra*-numbers it can be concluded that the size of these structures increases with the *Ra*-number.

Averaging the axial velocity component in azimuthal direction leads to two-dimensional mean flow fields as presented in Fig. 7. Again results for different values of *Ra* and *a* are shown. For all presented cases a mean flow, which rises in the center of the cylinder, was obtained. The size of these flow structures increases with the *Ra*-number.

We also investigated how the Nusselt number $Nu = \frac{H}{\kappa \Delta T}(\langle u_z T \rangle \Delta T u_b - \kappa \frac{\partial \langle T \rangle}{\partial z} \cdot \frac{\Delta T}{x_b}) = -a \frac{\partial \langle T \rangle_{\text{wall}}}{\partial z}$ scales with the *Ra*-number. Here $\langle \cdot \rangle$ denotes the average over an arbitrary horizontal cross section, while $\langle \cdot \rangle_{\text{wall}}$ denotes the average over the bottom or the top planes of the cylinder. Evaluating the *Nu*-number from DNS data obtained

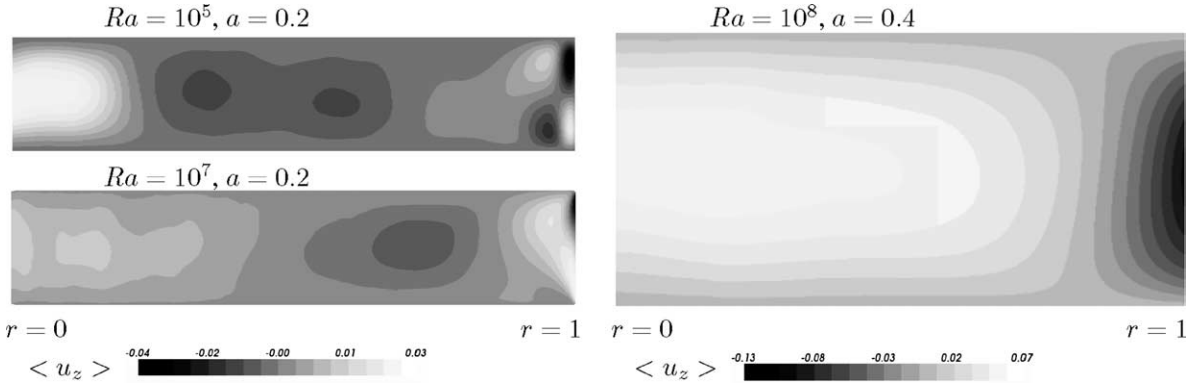

Fig. 7. Mean axial velocity $\langle u_z \rangle$ averaged in time and in the φ-direction.

for the cylinder of aspect ratio $a = 0.2$, the Nusselt numbers $Nu = 4.29$ ($Ra = 10^5$), $Nu = 8.81$ ($Ra = 10^6$), $Nu = 18.13$ ($Ra = 10^7$) were obtained. They fit the scaling law $Nu = 0.117 Ra^{0.313}$.

5.2.3. Spatial and temporal resolutions of the solution

The mean mesh size h must be of the same order as the Kolmogorov's scale $\eta = aPr^{1/2}(Nu - 1)^{-1/4}Ra^{-1/4}$, namely $h \sim \pi\eta$ in order to resolve all relevant turbulent scales in a DNS. For $a = 0.2$ and $Ra = 10^5$ for example, a mean mesh size $h = 2.19 \times 10^{-2}$ is needed while $a = 0.2$ and $Ra = 10^7$ leads to $h = 4.53 \times 10^{-3}$. This must be compared with the maximum mesh size of the mesh with $96 \times 256 \times 128$ grid points, i.e. $h_{\mathrm{DNS}} = \max_i(\Delta z_i \cdot r\Delta\varphi_i \cdot \Delta r_i)^{1/3} = 6.49 \times 10^{-3}$. Since $h_{\mathrm{DNS}} < h$ for $Ra = 10^5$, it is concluded that a fine enough spatial resolution was used to simulate the case $Ra = 10^5$, while the resolution is merely satisfactory for $Ra = 10^7$.

For temporal resolution we have two principal requirements: (i) the time step must be smaller than the Batchelor scale in order to resolve the smallest time scales; (ii) it has to be small enough to guarantee the numerical stability of the chosen discretization scheme (the Leapfrog–Euler scheme in our case). The Batchelor scale is equal to $\eta_T = a^{1/2}Pr^{1/2}(Nu - 1)^{-1/2}$. In the case $a = 0.2$ we get $\eta_T = 0.21$ ($Ra = 10^5$) and $\eta_T = 0.09$ ($Ra = 10^7$). Since we used the time step $\Delta t \approx 10^{-3}$ in our simulations due to stability reasons, we conclude that the time step is small enough to resolve the Batchelor scale.

References

[1] F. Heslot, B. Castaing, A. Libchaber, A transition to turbulence in helium gas, Phys. Rev. A 36 (1987) 5870–5873.
[2] B.I. Shraiman, E.D. Siggia, Heat transport in high-Rayleigh number convection, Phys. Rev. A 42 (1990) 3650–3653.
[3] E.D. Siggia, High Rayleigh number convection, Annu. Rev. Fluid Mech. 26 (1994) 137–168.
[4] X. Chavanne, F. Chillà, B. Chabaud, B. Castaing, B. Hebral, Turbulent Rayleigh–Bénard convection in gaseous and liquid He, Phys. Fluids 13 (2001) 1300–1320.
[5] S. Grossmann, D. Lohse, Scaling in thermal convection: a unifying theory, J. Fluid Mech. 407 (2000) 27–56.
[6] S.J. Kimmel, J.A. Domaradzki, Large Eddy Simulations of Rayleigh–Bénard convection using subgrid scale estimation model, Phys. Fluids 12 (2000) 169–184.
[7] G. Grötzbach, Direct numerical simulation of laminar and turbulent Bénard convection, J. Fluid Mech. 119 (1982) 27–53.
[8] R.M. Kerr, Rayleigh number scaling in numerical convection, J. Fluid Mech. 310 (1996) 139–179.
[9] R. Verzicco, R. Camussi, Numerical experiments on strongly turbulent thermal convection in a slender cylindrical cell, J. Fluid Mech. 477 (2003) 19–49.
[10] J.G.M. Eggels, F. Unger, M.H. Weiss, J. Westerweel, R.J. Adrian, R. Friedrich, F.T.M. Nieuwstadt, Fully developed turbulent pipe flow: a comparison between direct numerical simulation and experiment, J. Fluid Mech. 268 (1994) 175–209.
[11] F. Unger, Numerische Simulation turbulenter Rohrströmungen, Dissertation, Lehrstuhl fuer Fluidmechanik, TU Muenchen, 1994.
[12] H. Choi, P. Moin, J. Kim, Turbulent drug reduction: studies of feedback control and flow over riblets, Thermoscience Division, Dept. of Mech. Eng., Stanford, Report TF-55, 1992.

[13] A.G. Kravchenko, P. Moin, On the effect of numerical errors in large eddy simulations of turbulent flows, J. Comput. Phys. 131 (1997) 310–322.
[14] U. Schumann, Subgrid scale model for finite difference simulations of turbulent flows in plane channels and annuli, J. Comput. Phys. 18 (1975) 376–404.
[15] U. Schumann, Fast elliptic solvers and their application in fluid dynamics, in: W. Kollmann (Ed.), Computational Fluid Dynamics, Hemishere, Washington, 1980, pp. 376–404.
[16] A.J. Chorin, Numerical solution of the Navier–Stokes equations, Math. Comput. 22 (1968) 745–762.
[17] A.J. Chorin, On the convergence of discrete approximations to the Navier–Stokes equations, Math. Comput. 23 (1969) 341–353.
[18] O. Shishkina, C. Wagner, A fourth order finite volume scheme for turbulent flow simulations in cylindrical domains, Computers and Fluids, submitted for publication.
[19] O. Shishkina, C. Wagner, Stability conditions for the Leapfrog–Euler scheme with central spatial discretization of any order, J. Appl. Numer. Anal. Comput. Math. 1 (2004) 315–326.
[20] O. Shishkina, C. Wagner, Stability analysis of high-order finite volume schemes in turbulence simulations, in: G. Psihoyios (Ed.), NACoM-2003 Extended Abstracts, APU, Cambridge, UK, WILEY-VCH Verlag GmbH&Co. KGaA, Weinheim, 2003, pp. 158–161.
[21] B.E. Mitchell, S.K. Lele, P. Moin, Direct computation of the sound generated by an axisymmetric jet, AIAA J. 35 (10) (1997) 1574.
[22] K. Mohseni, T. Colonius, Numerical treatment of polar coordinate singularities, J. Comput. Phys. 157 (2000) 787–795.